OPEN

Correspondence and
requests for materials
should be addressed to
T.-W.L. (twlin@thu.
edu.tw)

High Energy Density Asymmetric Supercapacitor Based on NiOOH/Ni$_3$S$_2$/3D Graphene and Fe$_3$O$_4$/Graphene Composite Electrodes

Tsung-Wu Lin, Chao-Shuan Dai & Kuan-Chung Hung

Department of Chemistry, Tunghai University, No. 181, Sec. 3, Taichung Port Rd., Taichung City 40704, Taiwan.

The application of the composite of Ni$_3$S$_2$ nanoparticles and 3D graphene as a novel cathode material for supercapacitors is systematically investigated in this study. It is found that the electrode capacitance increases by up to 111% after the composite electrode is activated by the consecutive cyclic voltammetry scanning in 1 M KOH. Due to the synergistic effect, the capacitance and the diffusion coefficient of electrolyte ions of the activated composite electrode are ca. 3.7 and 6.5 times higher than those of the Ni$_3$S$_2$ electrode, respectively. Furthermore, the activated composite electrode exhibits an ultrahigh specific capacitance of 3296 F/g and great cycling stability at a current density of 16 A/g. To obtain the reasonable matching of cathode/anode electrodes, the composite of Fe$_3$O$_4$ nanoparticles and chemically reduced graphene oxide (Fe$_3$O$_4$/rGO) is synthesized as the anode material. The Fe$_3$O$_4$/rGO electrode exhibits the specific capacitance of 661 F/g at 1 A/g and excellent rate capability. More importantly, an asymmetric supercapacitor fabricated by two different composite electrodes can be operated reversibly between 0 and 1.6 V and obtain a high specific capacitance of 233 F/g at 5 mV/s, which delivers a maximum energy density of 82.5 Wh/kg at a power density of 930 W/kg.

G iven that its exceptionally high surface area (up to 2630 m²/g) and electrical conductivity (10^6 S/cm), graphene has been considered as the promising electrode material for the supercapacitors[1]. In addition to graphene, hierarchical nanostructured carbons (HNCs) containing 3D-interconnected macroporous/mesoporous and mesoporous/microporous structures have also attracted considerable attention because the electrode materials with hierarchical nanostructures offer the advantages of high surface area, synergistic inter-actions, and multiple functionalities[2–7]. Similar to other carbonaceous electrode materials such as activated carbon and carbon nanotubes (CNTs), the energy storage mechanism of graphene or HNC based electrodes mainly involves electrical double-layer capacitance. In the developments of graphene based supercapacitors, chemically reduced graphene oxide (rGO) is widely used as the substitute for pristine graphene due to the fact that the chemical exfoliation processes enable the mass production of graphene[8]. However, the outstanding properties of graphene are significantly weakened in rGO because the re-stacking of rGO via the strong π-π interaction greatly loses the useful surface area and the residual defects in rGO significantly reduce the conduc-tivity of graphene. The aforementioned limitations greatly impair the electrochemical performances of rGO electrodes; as a result, the supercapacitors based on rGO electrodes usually show that the specific capacitances (C$_m$) range from 100 to 200 F/g in the aqueous electrolytes[9–11].

Due to the limited capacitance of graphene-based electrodes, much attention has been paid to exploit electrode materials with pseudocapacitive properties such as metal oxide[12–15] and conducting polymers[16–19]. Recently, it has been demonstrated that nickel sulfides (NiS) with various nanostructures display high capacitive performance and great long-term stability, suggesting that NiS is a promising supercapacitor electrode material[20–22]. Although metal oxides or sulfides usually show the higher C$_m$ values than graphene-based electrodes, they generally suffer from serious particle agglomeration and poor electrical conductivity, which significantly restricts their applica-tions in supercapacitors. To fully utilize all the potential advantages of graphene and pseudocapacitive materials, much effort has been devoted to the studies of the composites of graphene and pseudocapacitive materials. Many studies have demonstrated that the composite electrodes exhibit the improved capacitive performances compared with the electrodes consisting of the individual components of graphene or pseudocapacitive materials[23]. For the

composite electrode, the enhancements of the electrochemical performances mainly benefit from the introduction of graphene. The graphene in a composite electrode serves as the multifunctional support for anchoring electroactive materials. From the viewpoint of graphene properties, graphene can be considered as an ideal building block in composite electrodes for supercapacitors. Firstly, the high surface area of graphene can induce the uniform growth of nanomaterials on the graphene surface. On the other hand, the electroactive nanomaterials deposited on graphene suppress the aggregation and the re-stacking of graphene, thus increasing the available surface area of the graphene. Secondly, the high conductivity of graphene enables fast electron transport through the underlying graphene layers to electroactive nanomaterials. Finally, the great mechanical flexibility of graphene improves the cycle stability and rate capability of composite electrode for supercapacitors[24]. Due to the aforementioned synergistic effects of graphene and electroactive nanomaterials, the enhancement of capacitive performance of composite electrode is significant.

Over the past years, an asymmetric supercapacitor (ASC) has aroused more and more attention because it can deliver a remarkably high power density and an ultrahigh energy density. By combining complementary potential windows of the cathode and anode, the ASC can be operated in a wider voltage window and thus exhibits the greater energy density compared with symmetric supercapacitors[25]. In this study, we report the fabrication of high energy density ASC assembled with highly capacitive graphene-based composite cathode and anode. The composite of Ni_3S_2 nanoparticles and 3D graphene (Ni_3S_2/3D-G) synthesized by glucose-assisted hydrothermal method is used as the cathode for ASCs. This novel hybrid electrode exhibits an ultrahigh capacitance of 3296 F/g and good cycling stability at a high current density of 16 A/g. To satisfy the capacitance balance between the cathode and anode, the composite of Fe_3O_4 nanoparticles and rGO (Fe_3O_4/rGO) synthesized by a hydrothermal method serves as a highly capacitive anode material. Due to the synergistic effects of conductive rGO and Fe_3O_4 nanoparticles, the anode shows a high capacitance of 661 F/g at a current density of 1 A/g and a good rate capability. Finally, the ASC assembled with two different composite electrodes can deliver a high energy density of 82.5 Wh/kg at a power density of 930 W/kg.

Results

Material characterization of Ni_3S_2/3D-G. As shown in Figure S1a and S1b, scanning electron microscopy (SEM) images reveal that the as-grown graphene films adhere to the surface of nickel foam. Due to the difference between the thermal expansion coefficients of nickel and graphene, ripples and wrinkles of the graphene films are observed[26]. The thickness of the as-grown graphene films on Ni foam was estimated by Raman spectroscopy. As shown in Figure S1c, the peaks at around 1579 and 2660 cm^{-1} correspond to the G and 2D bands of graphene, respectively. Furthermore, the disorder-induced D band at ca. 1350 cm^{-1} is not observed, thus indicating the high quality of as-grown graphene. On the basis of the G to 2D peak intensity ratios, the as-grown 3D-G consists of bi- to few-layer graphene sheets[27]. The non-uniformity is attributed to the polycrystalline nature of the nickel foam, in which individual nickel grains may independently affect the thickness of the graphene film during chemical vapor deposition (CVD)[27]. The morphology of the 3D-G sample after the hydrothermal reaction was also characterized by SEM. As shown in Figure 1a and 1b, the graphene surface is uniformly and densely decorated with the nanoparticles. In the high-magnification SEM (Figure 1c), it is found that the morphology of a particle is irregular and the diameter of the irregularly shaped particle is ca. 1 μm. The transmission electron microscopy (TEM) image of the composite sample confirm that conductive graphene can serve as the substrate where small nanoparticles are self-assembled into irregularly shaped particles as indicated by the red circles in
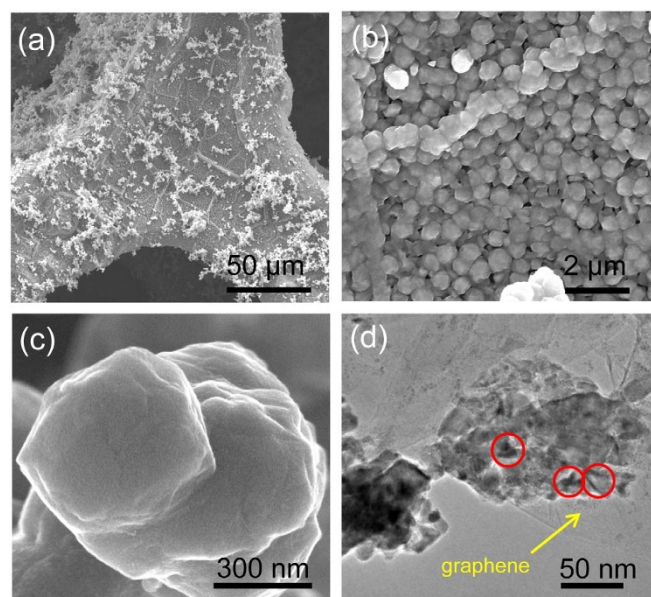

Figure 1 | Morphology characterizations of Ni_3S_2/3D-G. (a)–(c) SEM images and (d) TEM image of Ni_3S_2/3D-G.

Figure 1d, which is consistent with our previous study[28]. Our previous work has verified that the use of glucose and the CNTs with high surface area in the hydrothermal reaction plays a crucial role in the formation of the hierarchical structure. In the hydrothermal reaction, glucose not only mediates the formation of nanoparticles with smaller size but also meanwhile serves as a binder to assist the assembly of nanoparticles and their subsequent growth on the graphene surface[29]. On the other hand, the graphene with high surface area can serve as a good substrate to avoid the aggregation of deposited material[30,31]. As evidenced by our control experiment, when 3D-G is absent in the hydrothermal synthesis, the diameters of the as-synthesized particles range from 0.5 to 4 μm (Figure S2). The drastic difference in particle size highlights the important role of 3D-G as an effective substrate for the growth of nanomaterials.

To further characterize the identity and structure of the composite sample, X-ray powder diffraction (XRD) and Raman measurements were carried out. As shown Figure 2a, the sharp peak at $2\theta = 26.3°$ indicates that the interlayer spacing inside the few-layered graphene sheet has a structure similar to that of normal graphite[32]. Except the (002) reflection of graphene, all the identified peaks can be attributed to the Ni_3S_2 phase (JCPDS card No. 30-0863). Figure 2b shows the Raman spectrum of the composite sample. In the low-frequency region, the three peaks at 308, 328 and 350 cm^{-1} can be assigned to the Raman characteristic bands of Ni_3S_2[33]. Furthermore, it is noted that the spectrum profile in the high-frequency region for composite sample is totally different from that of pristine 3D-G (Figure S1c). The presence of amorphous carbon in the composite sample is evidenced by the new peak emerged at ca.1370 cm^{-1} (D band) and the broad G band at 1568 cm^{-1}. The amorphous carbon is derived from the hydrothermal carbonization of glucose[34,35]. To analyze the surface composition of the composite sample, we performed X-ray photoelectron spectroscopy (XPS) analysis. Figure 2c and 2d show the XPS results for elemental Ni and C measured from the composite sample. The intense peak at around 856 eV can be deconvoluted into eight components using published fitting information[36,37]. It is noteworthy that the peak located at 852.6 eV can be assigned to the characteristic peak of Ni_3S_2. Furthermore, other seven peaks ranging from 854.5 to 861.3 eV suggest the presence of nickel oxyhydroxide (NiOOH) on the surface of Ni_3S_2. The formation of NiOOH could be due to the oxidation of Ni_3S_2 in air[38]. Figure 2d displays that the C 1s
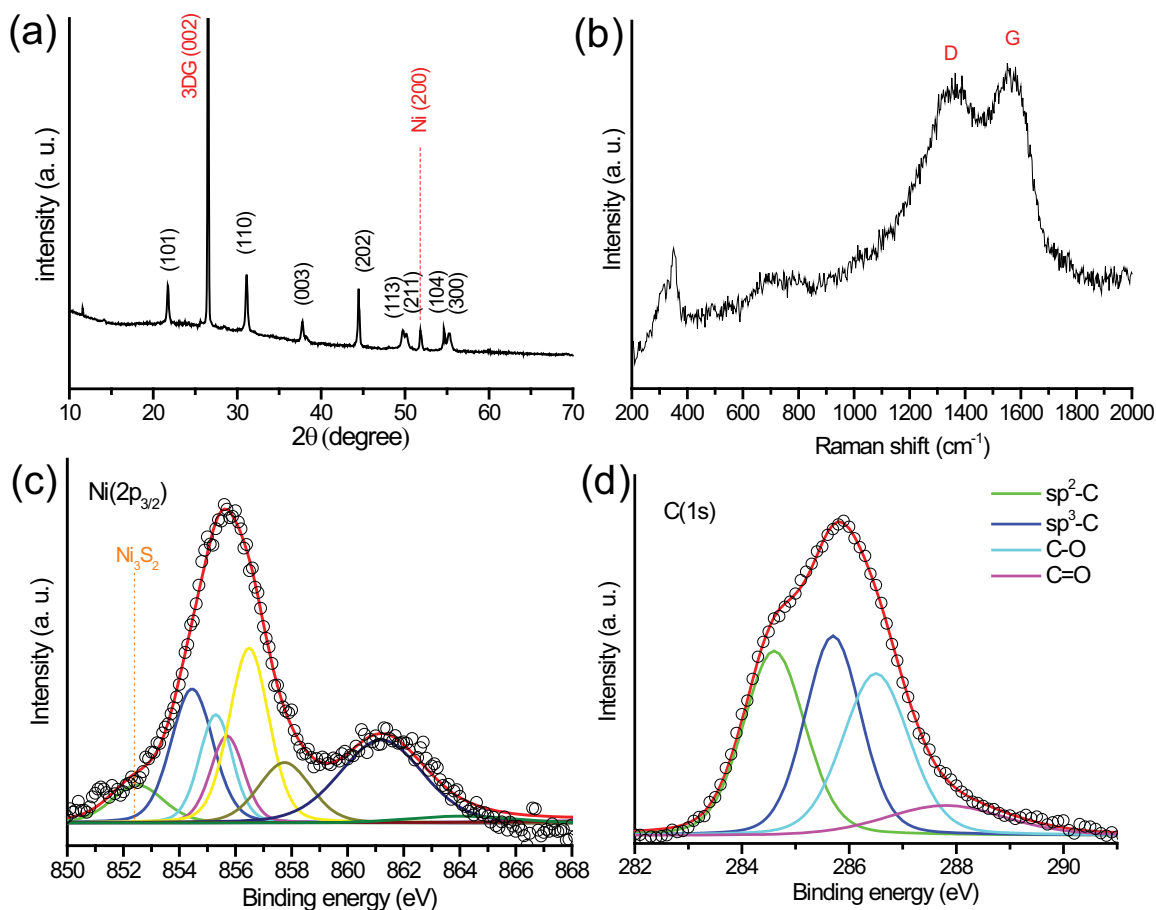
Figure 2 | Composition characterizations of Ni₃S₂/3D-G. (a) XRD pattern (b) Raman spectrum, and (c)–(d) XPS spectra of Ni₃S₂/3D-G.

spectrum with a feature of a broad band centered at 285.7 eV can be deconvoluted into four peaks. The peaks at 284.6 and 285.7 eV are attributed to sp²- and sp³-hybridized carbon atoms, respectively whereas the peaks at 286.5 and 287.8 eV are carbon atoms bound to one oxygen atom by a single bond and a double bond, respectively[39]. The aforementioned four different forms of chemical bonding are originated from the amorphous carbon[35,40]. On the basis of the microscopic and spectroscopic data, we can conclude that the Ni_3S_2 nanoparticles successfully deposit on graphene substrate and their surface is partially oxidized to NiOOH and is covered by a thin layer of amorphous carbon.

Electrochemical performances of Ni₃S₂/3D-G Electrode. Our previous studies have proved that the consecutive cyclic voltammetry (CV) scanning in a KOH solution induces the morphological change of the composite electrode synthesized by glucose-assisted hydrothermal method, which further enhances the capacitive performance of the electrode[28]. This activation process involving 400 CV cycles at 50 mV/s in 1 M KOH is also performed in the current work. Figure 3a shows the CV curves of the electrodes of 3D-G, as-synthesized Ni_3S_2/3D-G and the activated Ni_3S_2/3D-G measured at a scan rate of 5 mV/s in 1 M KOH. The CV curve of the Ni_3S_2/3D-G electrode exhibits a pair of redox peaks in the potential range from 0 to 0.6 V and the redox peaks at around 0.45 and 0.23 V can be attributed to the reversible redox reactions of Ni(II) $\leftrightarrow$ Ni(III)[20,21]. Furthermore, the redox peak current of the Ni_3S_2/3D-G electrode is much larger than that of 3D-G electrode. The area surrounded by the CV curve is dramatically enhanced by the combination of Ni_3S_2 nanoparticles with 3D-G. This result suggests that the large capacitance of the composite electrode is mainly derived from the pseudocapacitance of the electrochemically active Ni_3S_2 nanoparti-

cles instead of double-layer capacitance from the 3D-G. It is noteworthy that the Ni_3S_2/3D-G electrode after the activation process shows a larger area under the CV curve compared with as-synthesized one. The C_m value of the composite electrode can be estimated by integrating the area under the reduction peak of a stable CV and then dividing by the scan rate (v), the mass of the active material (m) in the electrode and the potential window ($V_a - V_c$) according to the following equation.

$$C_m = \frac{1}{mv(V_a - V_c)} \int_{V_a}^{V_c} I(V)dV \tag{1}$$

After the activation process, the C_m value of the composite electrode is increased from 1120 to 2362 F/g and the increasing percentage of the C_m value is ca. 111%. To further emphasize the effect of combining Ni_3S_2 nanoparticles with 3D-G on electrode performance, the comparisons between Ni_3S_2 electrode and Ni_3S_2/3D-G are made. Figure 3b and Figure S2c show the CV curves of the activated Ni_3S_2/3D-G and Ni_3S_2 electrodes at the different scan rates, respectively. It is noteworthy that the C_m values of the activated Ni_3S_2/3D-G electrode obtained at 5, 10, 20 and 50 mV/s are 2362, 2250, 2068 and 1859 F/g, respectively and are ca. 3.7 times higher than those of the Ni_3S_2 electrode. For example, at a scan rate of 50 mV/s, the C_m value of the activated Ni_3S_2/3D-G electrode is 1859 F/g whereas the pure Ni_3S_2 electrode shows a much lower capacitance of 494 F/g. The relatively large C_m values of the composite electrode could be attributed to the fact that the small sizes of Ni_3S_2 nanoparticles on 3D-G allow nearly full utilization of the electrode materials[41,42]. On the other hand, the inset in Figure 3b shows that the cathodic peak current increases linearly with the square root of the scan rate, indicating that the redox reaction at electrode/electrolyte interface belongs to diffusion-controlled
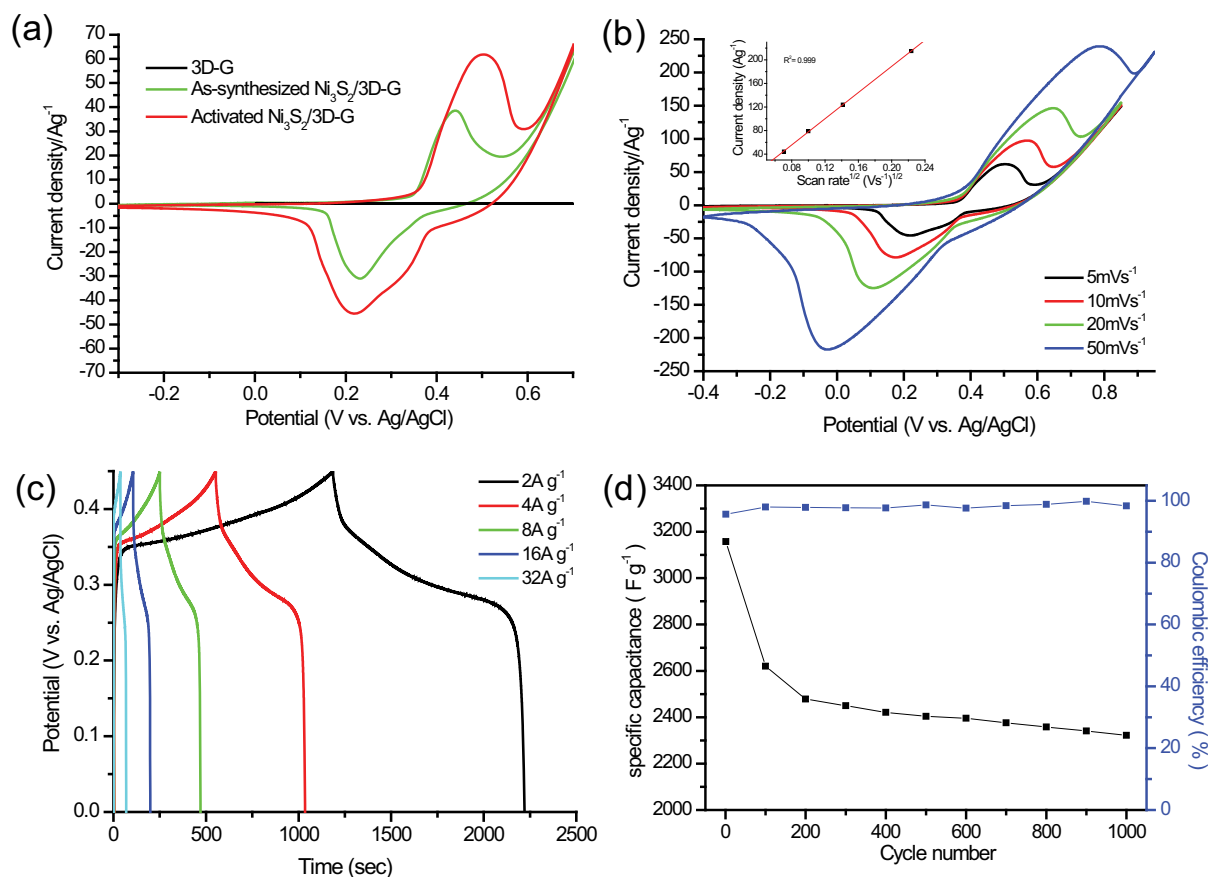
Figure 3 | Electrochemical performances of Ni₃S₂/3D-G electrode. (a) CV curves of the 3D-G and Ni₃S₂/3D-G electrodes measured at a scan rate of 5 mV/s. (b) CV curves of the activated Ni₃S₂/3D-G electrode recorded at the different scan rates (5, 10, 20 and 50 mV/s) in 1 M KOH. The inset shows that the variation of the current density of cathodic peak as a function of the square root of scan rate. (c) Charge-discharge curves of the activated Ni₃S₂/3D-G electrode at different current densities (2, 4, 8, 16 and 32 A/g) in 1 M KOH. (d) The variations in specific capacitance and Coulombic efficiency of the activated Ni₃S₂/3D-G electrode as a function of cycle number at the current density of 16 A/g.

process and therefore the charge-transfer reaction in the interface is relatively rapid. According to the slopes shown in the insets of Figure 3b and the Figure S2c, the diffusion coefficient of electrolyte ions for the activated Ni₃S₂/3D-G electrode is 6.5 times higher than that of the Ni₃S₂ electrode. This result suggests that the Ni₃S₂/3D-G electrode has the efficient and fast ion diffusion due to the open pore system and nano-sized morphology of the composite[14,43]. In Figure 3c, the galvanostatic charge/discharge curves of the activated Ni₃S₂/3D-G electrode obtained at different current densities exhibit a non-linear profile as expected for the pseudocapacitive electrode. The C_m value can be alternatively estimated from the discharge section according to the equation (2):

$$C_m = \frac{I \times \Delta t}{m \times \Delta V} \qquad (2)$$

where I, Δt, ΔV, and m represent discharge current, discharge time, potential window, and the mass of Ni₃S₂ in the composite, respectively. The C_m values of the activated Ni₃S₂/3D-G electrode are calculated to be 4598, 4284, 3897, 3296 and 2261 F/g at 2, 4, 8, 16 and 32 A/g, respectively. It is noteworthy that the C_m value of the activated Ni₃S₂/3D-G electrode is much higher than the electrodes constructed by NiS nanoflakes (664 F/g at 4 A/g)[20], NiS hollow spheres (927 F/g at 4.08 A/g)[21], NiS nanoparticles (893 F/g at 5 A/g)[22], Ni₃S₂/CNT composite (514 F/g at 4 A/g)[44], NiS/graphene oxide (800 F/g at 1 A/g)[45], and Ni₃S₂/rGO (1424 F/g at 0.75 A/g)[46]. To get more information about the electrochemical stability of the composite electrode, the consecutive charge–discharge cycles were performed at a high current density of 16 A/g. As shown in

Figure 3d, the C_m retention of Ni₃S₂/3D-G is 74% after 1000 cycles, which shows the reasonable cycling stability. The decrease in the C_m value of Ni₃S₂/3D-G after a long-term test can be attributed the exfoliation of Ni₃S₂/3D-G from Ni-foam as evidenced by SEM observations (Figure S3). Furthermore, the composite electrode exhibits nearly 100% Coulombic efficiency over the entire cycling test.

To understand the origin of the increase in capacitance of Ni₃S₂/3D-G electrode after the activation process, we analyzed the electrode morphology and its surface composition. As shown in Figure 4a, the SEM image of the activated Ni₃S₂/3D-G electrode reveals that the electrode surface become very rough. Furthermore, Figure 4b and 4c show the XPS results for elemental Ni and C measured from the activated composite electrode. It is noteworthy that the Ni₃S₂ peak at 852.6 eV disappears and only the characteristic peaks of NiOOH are observed. Furthermore, no signal of the elemental S can be detected in the surface of activated electrode as shown in Figure S4. These results suggest that the surface composition of electrode is converted from Ni₃S₂ into NiOOH and thus the activated composite electrode is referred to as NiOOH/Ni₃S₂/3D-G in the subsequent discussion. The formation of NiOOH during the activation process is consistent with the previous study of using Ni₃S₂ nanorods/Ni foam composite electrode as a catalyst for the oxygen evolution reaction in a alkaline solution[36]. Furthermore, the C1s spectrum profile of the NiOOH/Ni₃S₂/3D-G electrode is significantly different from that of the as-synthesized Ni₃S₂/3D-G. It is noteworthy that the peak attributed to sp³-hybridized carbon atoms (at 285.7 eV) nearly disappears as shown in Figure 4c. Moreover, the
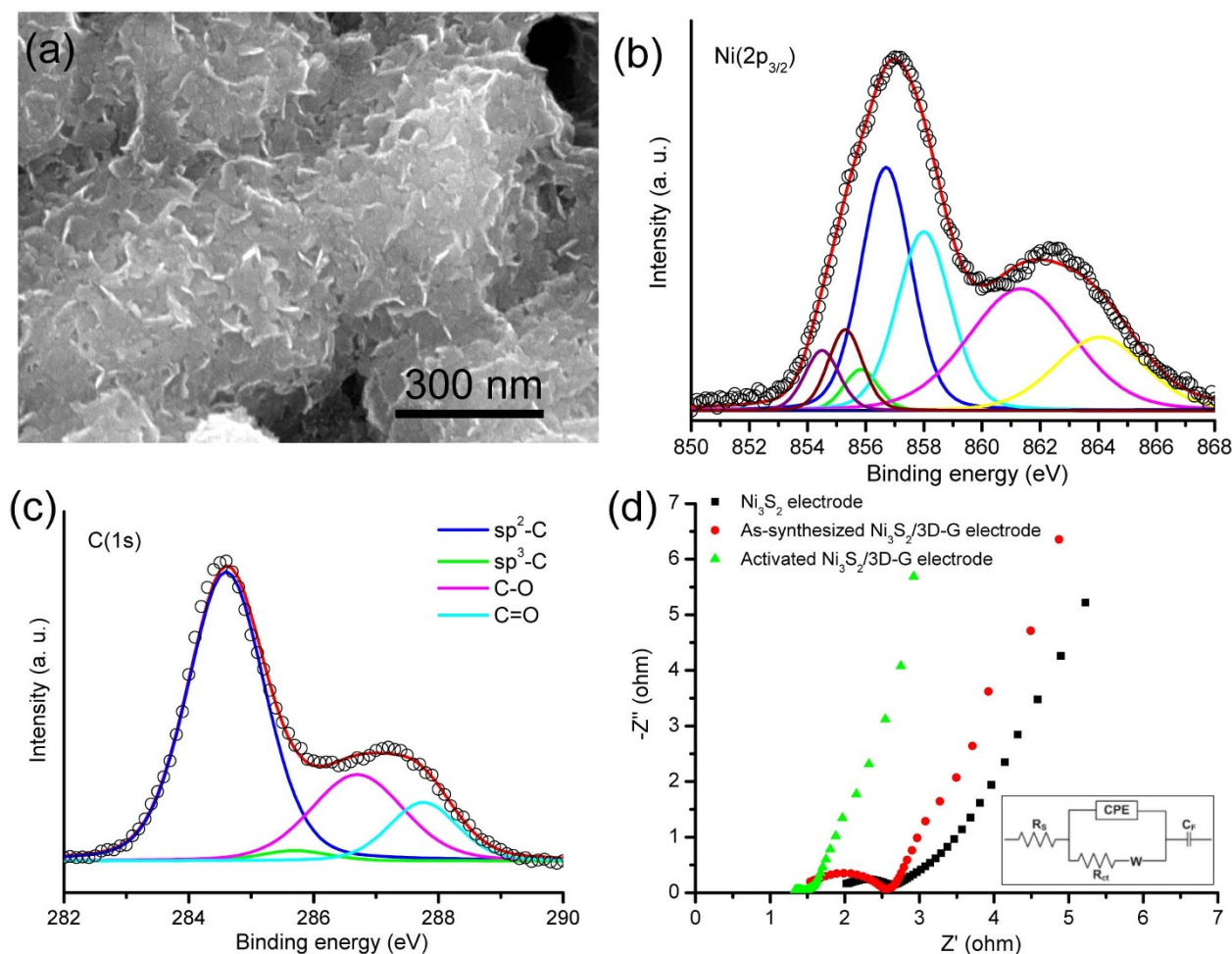
Figure 4 | Surface analysis of the activated Ni₃S₂/3D-G electrode. (a) SEM image and (b)–(c) XPS spectra of the activated Ni$_3$S$_2$/3D-G electrode. (d) Nyquist plots of the pure Ni$_3$S$_2$, as-synthesized Ni$_3$S$_2$/3D-G and NiOOH/Ni$_3$S$_2$/3D-G electrodes. The inset shows the equivalent circuit used to simulate the Nyquist plots. In the equivalent circuit, CPE represents the constant phase element accounting for a double-layer capacitance, Z$_W$ is the Warburg impedance, and C$_F$ is the Faradaic pseudocapacitor.

atomic ratio of Ni to C in the NiOOH/Ni$_3$S$_2$/3D-G electrode is 0.227 : 1 whereas that in the Ni$_3$S$_2$/3D-G electrode is 0.07 : 1. Due to the decrease in the peak intensity of sp^3-hybridized carbon atoms and the increase in Ni content, it is suggested that the amorphous carbon is partially removed from the electrode surface via the consecutive CV scanning in a KOH solution. The change in electrode morphology and the capacitance enhancement after the activation process can be attributed to the combined effect of the removal of amorphous carbon and the formation of NiOOH. The partial removal of amorphous carbon from the electrode surface leads to the increase in the exposure of the active sites in the composite electrode. Furthermore, due to the fact that NiOOH and Ni$_3$S$_2$ co-exist in the electrode, these electroactive materials can both give the contributions to the electrode capacitance. As a result, the possible pseudocapacitive reaction mechanisms are described by the following equations[20,21,47]:

$$Ni_3S_2 + 3OH^- \leftrightarrow Ni_3S_2(OH)_3 + 3e^- \qquad (3)$$

$$Ni(OH)_2 + OH^- \leftrightarrow NiOOH + H_2O + e^- \qquad (4)$$
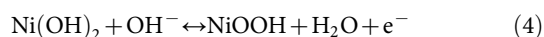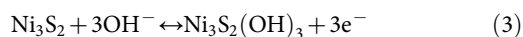
To further understand the mechanism behind the excellent capacitive performance of the NiOOH/Ni$_3$S$_2$/3D-G electrode, the electrochemical impedance spectroscopy (EIS) measurements were performed at a frequency range from 10 kHz to 0.01 Hz. As shown in Figure 4d, each Nyquist plot consists of a semicircle in the high frequency region and a straight line in the low frequency region. The intercept at real axis represents the combined resistance (R$_s$) including ionic resistance of electrolyte, intrinsic resistance of substrate, and contact resistance at the interface of active material/current collector whereas the diameter of a semicircle corresponds to the charge transfer resistance (R$_{ct}$) at the electrode/electrolyte interface[25]. The R$_s$ and R$_{ct}$ values can be evaluated by fitting the EIS spectra based on the equivalent circuit proposed in the inset of Figure 4d. The R$_{ct}$ values of the Ni$_3$S$_2$/3D-G electrode and NiOOH/Ni$_3$S$_2$/3D-G electrode are 844 and 315 mΩ, respectively, being much smaller than that of the pure Ni$_3$S$_2$ electrode (947 mΩ). Therefore, the composite electrode shows faster reaction kinetics than the Ni$_3$S$_2$ electrode. Furthermore, the combination of Ni$_3$S$_2$ with highly conductive graphene leads to the decrease in R$_s$ value. For example, the R$_s$ value of the NiOOH/Ni$_3$S$_2$/3D-G electrode is 1.23 Ω whereas the pure Ni$_3$S$_2$ electrode shows a higher resistance of 1.78 Ω. The aforementioned EIS studies verify that the synergistic effect of the electrochemically active nanoparticles and the conductive 3D-G is responsible for enhancing the capacitive performance of the NiOOH/Ni$_3$S$_2$/3D-G electrode.

Material and electrochemical characterizations of Fe₃O₄/rGO electrode. To evaluate the capacitive performance of the Ni$_3$S$_2$/3D-G electrode in a full-cell configuration, it is attempted to fabricate an ASC device. Because the Ni$_3$S$_2$/3D-G electrode exhibits the exceptionally high C$_m$ value, the reasonable matching of cathode/

anode becomes extremely important for obtaining an ASC with a high energy density. As a result, exploring the anode material with high capacitance becomes a huge challenge. In the current study, we synthesize the Fe_3O_4/rGO composite as the material for anode. Figure 5a and 5b show low- and high magnification TEM images of Fe_3O_4/rGO composite, respectively. It is evident that the conductive rGO can serve as the substrate where Fe_3O_4 nanoparticles with the averaged diameter of 5 nm densely deposit. No apparent aggregation of Fe_3O_4 nanoparticles on the rGO is observed; in contrast, Fe_3O_4 nanoparticles aggregate to large particles in the absence of graphene (Figure S5a). To further characterize the composition and structure of the composite sample, energy dispersive X-ray spectroscopy (EDS) and XRD measurements were carried out. As shown in Figure 5c, the EDS analysis of the composite sample reveals the presence of C, O, Si, and Fe elements. Furthermore, the XRD pattern of the Fe_3O_4/rGO composite shown in Figure 5d corresponds to the magnetite Fe_3O_4 (JCPDS card No. 72-2302). On the basis of the aforementioned data, we can conclude that the Fe_3O_4/rGO composite is successfully synthesized.

To further emphasize the effect of combining Fe_3O_4 nanoparticles with rGO on electrode performance, the comparisons among pure Fe_3O_4, pure rGO and Fe_3O_4/rGO electrodes are made. Figure 6a shows the CV curves of the electrodes of Fe_3O_4, rGO and Fe_3O_4/rGO measured at a scan rate of 20 mV/s in 1 M KOH. The CV curve of the rGO electrode measured in the potential range from 0 to −1.2 V exhibits nearly rectangular-like shape, which clearly manifests the electrical double layer capacitive behavior. In contrast, the

CV curves of Fe_3O_4/rGO and pure Fe_3O_4 electrodes exhibit a pair of redox peaks, which corresponds to the reversible reactions of Fe(II) ↔ Fe(III)[48]. It is noteworthy that the Fe_3O_4/rGO electrode shows a larger area under the CV curve than two pure electrodes and thus possesses the superior capacitive property. The C_m values of the Fe_3O_4/rGO electrode obtained at 5, 10, 20 and 50 mV/s are 447, 461, 412, and 303 F/g, respectively (Figure S6). A large specific capacitance of the composite electrode is mainly derived from the pseudocapacitance of the electrochemically active Fe_3O_4 nanoparticles instead of double-layer capacitance from the rGO. In Figure 6b, the galvanostatic charge/discharge curve of the rGO electrode measured at the current density of 1 A/g is symmetric and linear whereas the Fe_3O_4 and Fe_3O_4/rGO electrodes exhibit the non-linear curves. The difference in curve profile is attributed to the distinct energy storage mechanisms. The C_m values measured at 1 A/g for rGO, Fe_3O_4 and Fe_3O_4/rGO electrodes are 228, 325.7 and 661.3 F/g, respectively. The Fe_3O_4/rGO electrode exhibits the higher capacitance than pure rGO and Fe_3O_4 electrodes due to the fact that perfect combination of Fe_3O_4 and rGO not only prevents the agglomeration of nanoparticles but also enables fast electron transport through the underlying rGO layers to Fe_3O_4 nanoparticles[48,49]. Figure 6c and Figure S5c show the galvanostatic charge/discharge curves of the Fe_3O_4/rGO and Fe_3O_4 electrodes obtained at different current densities, respectively. The C_m values of the Fe_3O_4/rGO electrode are calculated to be 661.3, 536.8, 475.6 and 430.4 F/g at 1, 2, 4 and 8 A/g, respectively. Furthermore, the Fe_3O_4/rGO electrode shows the better rate capability than pure Fe_3O_4 electrode as shown in

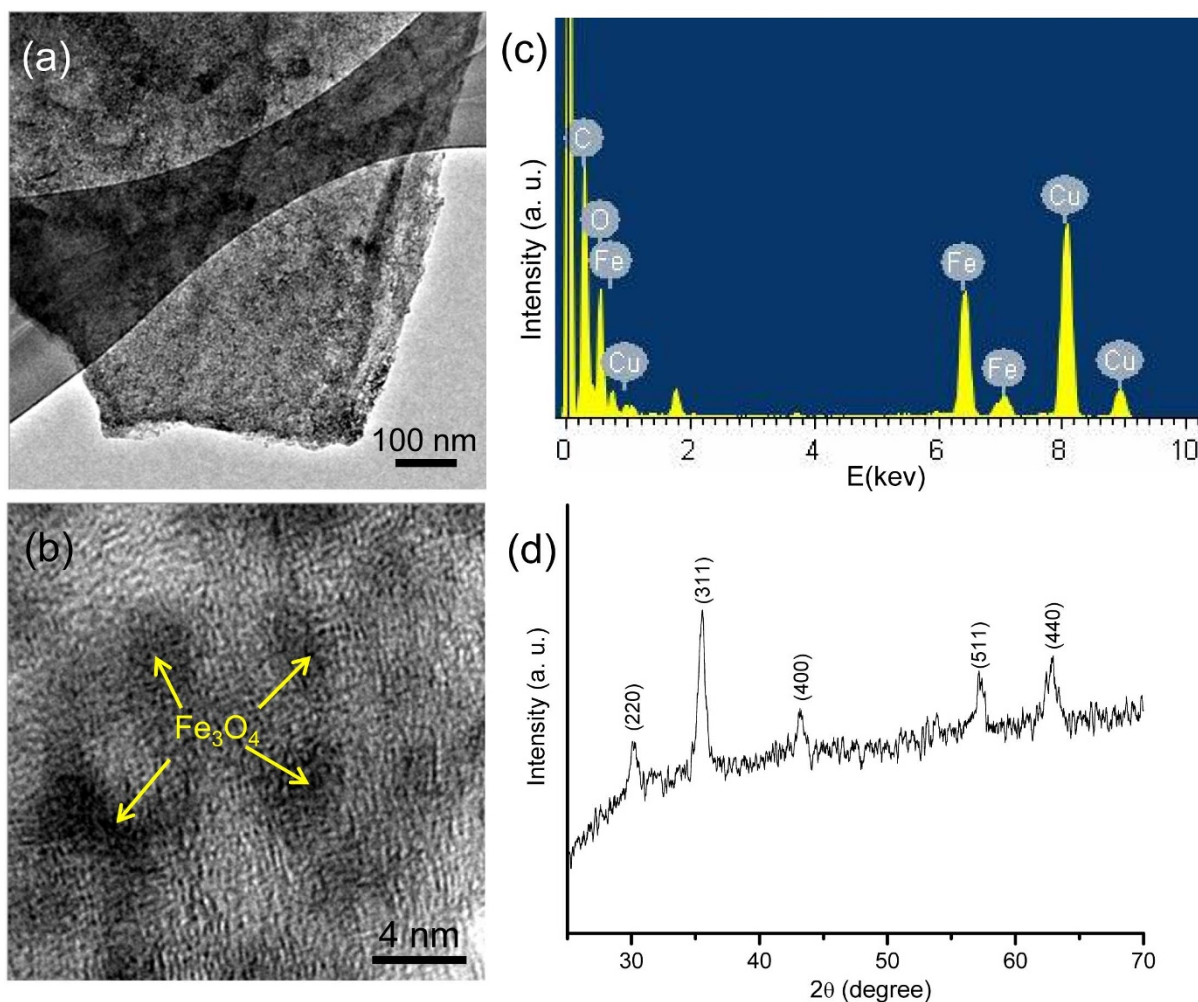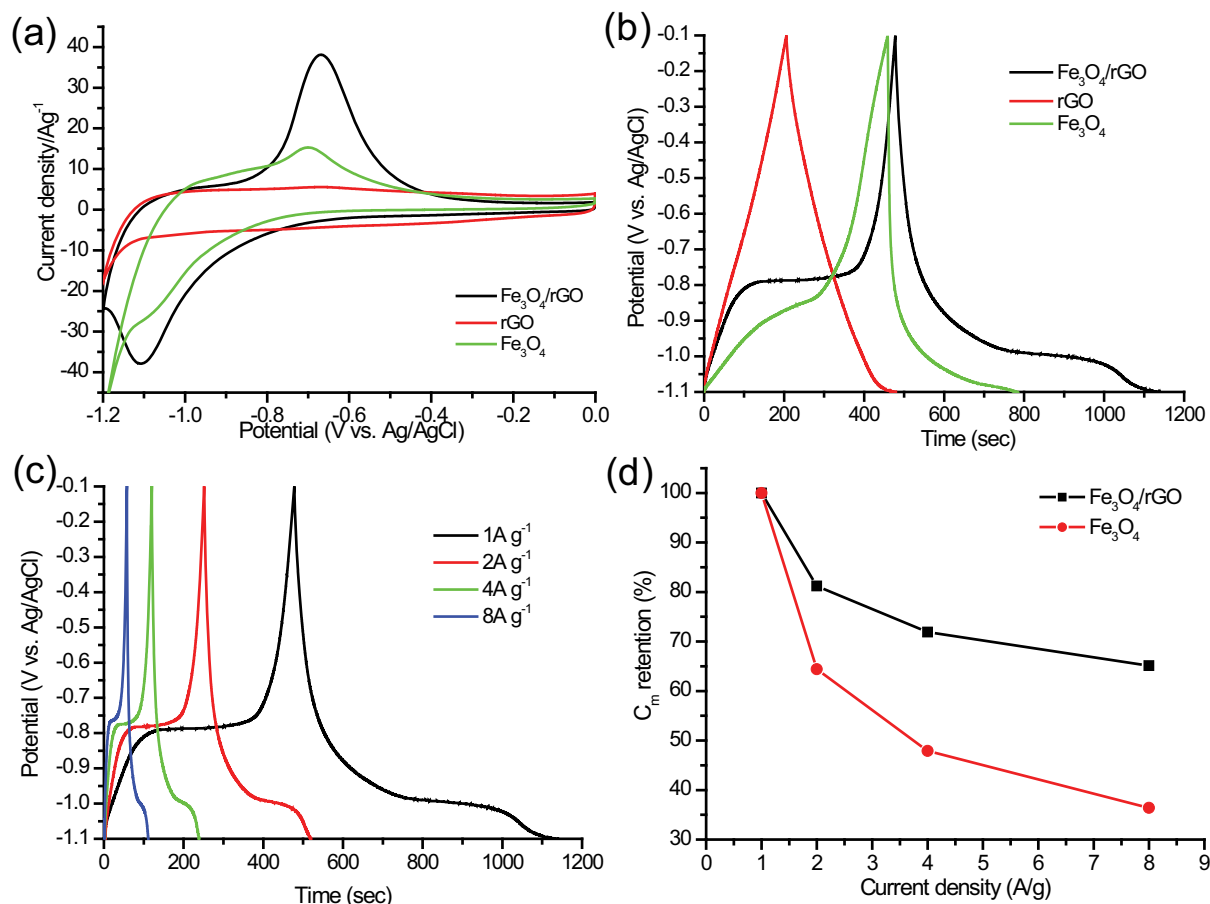**Figure 5 | Material characterizations of Fe_3O_4/rGO composite.** (a)–(b) TEM images, (c) EDS spectrum and (d) XRD pattern of Fe_3O_4/rGO.

Figure 6 | Electrochemical performances of Fe₃O₄/rGO electrode. (a) CV curves (measured at 20 mV/s) and (b) Charge-discharge curves (measured at 1 A/g) of the Fe_3O_4, rGO and Fe_3O_4/rGO electrodes. (c) Charge-discharge curves of the Fe_3O_4/rGO electrode at different current densities (1, 2, 4 and 8 A/g) in 1 M KOH. (d) Capacitance retentions of the Fe_3O_4 and Fe_3O_4/rGO electrodes as a function of discharge current densities.

Figure 6d. It is noteworthy that the Fe_3O_4/rGO electrode in the current work has a higher C_m value compared with the previously reported Fe_3O_4/rGO electrodes[50–53].

Electrochemical performances of the ASC based on Ni₃S₂/3D-G and Fe₃O₄/rGO composite electrodes. Since we successfully develop the highly capacitive cathode and anode, the ASC is fabricated by using the NiOOH/Ni₃S₂/3D-G as the cathode and Fe₃O₄/rGO as the anode (denoted as NiOOH/Ni₃S₂/3D-G//Fe₃O₄/rGO). To obtain a well electrochemical performance for ASC, the charge balance between the cathode and the anode should be satisfied. Therefore, on the basis of the C_m values and potential windows of two composite electrodes, the optimum loading mass ratio of Ni₃S₂ to Fe₃O₄/rGO is 0.26 : 1. As shown in Figure 7a, the CV curves of NiOOH/Ni₃S₂/3D-G//Fe₃O₄/rGO device measured at different scan rates exhibit the redox humps, which may be attributed to the contribution from the pseudocapacitive electrodes. It is noteworthy that the C_m values of the NiOOH/Ni₃S₂/3D-G//Fe₃O₄/rGO device obtained at 5, 10, 20 and 50 mV/s are 233, 214, 192 and 167 F/g, respectively. The galvanostatic charge/discharge curves of the ASC were measured at the current densities from 1 to 16 A/g in a potential window of 0–1.6 V. As shown in Figure 7b, the perfectly linear charge/discharge curves of electrical double layer capacitors are not obtained in the NiOOH/Ni₃S₂/3D-G//Fe₃O₄/rGO device, which indicates the pseudocapacitive nature of the supercapacitor. Furthermore, the C_m values of NiOOH/Ni₃S₂/3D-G//Fe₃O₄/rGO device are calculated to be 170, 158, 148, 136 and 118 F/g at 1, 2, 4, 8 and 16 A/g, respectively. Even at a high current density of 16 A/g, ca. 70% capacitance retention is observed. In

Figure 7c, Ragone plot related to power densities (P) and energy densities (E) is further used to evaluate the performance of NiOOH/Ni₃S₂/3D-G//Fe₃O₄/rGO device. The P and E values of the ASC were calculated by the following equations:

$$E = 1/2 \times C_m \times (\Delta V)^2 \tag{5}$$

$$P = E/\Delta t \tag{6}$$

where C_m is calculated based on the CV curve of the ASC device, ΔV is the operating voltage of the cell, and Δt is the discharge time. The NiOOH/Ni₃S₂/3D-G//Fe₃O₄/rGO device can deliver a high energy density of 82.5 Wh/kg at a power density of 930 W/kg and still maintain 63.1 Wh/kg at a high power density of 6.9 kW/kg. It is noteworthy that the NiOOH/Ni₃S₂/3D-G//Fe₃O₄/rGO device exhibits the superior energy density to the ASCs based on pseudocapacitive cathodes and anodes such as H-CoOx@Ni(OH)₂//RGO@Fe₃O₄ (45.3 Wh/kg at 1010 W/kg)[53], MnO₂/FeOOH (24 Wh/kg at 450 W/kg)[54], MnO₂//Fe₃O₄ (8.1 Wh/kg at 10.2 kW/kg)[55], Ni(OH)₂//ZnFe₂O₄ (14 Wh/kg at 209 W/kg)[56], LiMn₂O₄//MnFe₂O₄ (10 Wh/kg at 300 W/kg)[57], LiMn₂O₄//MnO₂/CNT (56 Wh/kg at 300 W/kg)[58]. To test the electrochemical stability of the NiOOH/Ni₃S₂/3D-G//Fe₃O₄/rGO device, consecutive charge–discharge cycles were performed at a current density of 1 A/g. However, ca. 74% decrease in capacitance is observed after 2000 charge/discharge cycles (Figure 7d). The instability of NiOOH/Ni₃S₂/3D-G//Fe₃O₄/rGO device mainly originates from the decay of Fe₃O₄/rGO electrode. After 2000 charge/discharge cycles, the C_m value of Fe₃O₄/rGO electrode is decreased to 106 F/g as shown in Figure S7. As a result, the charge balance between the cathode and the

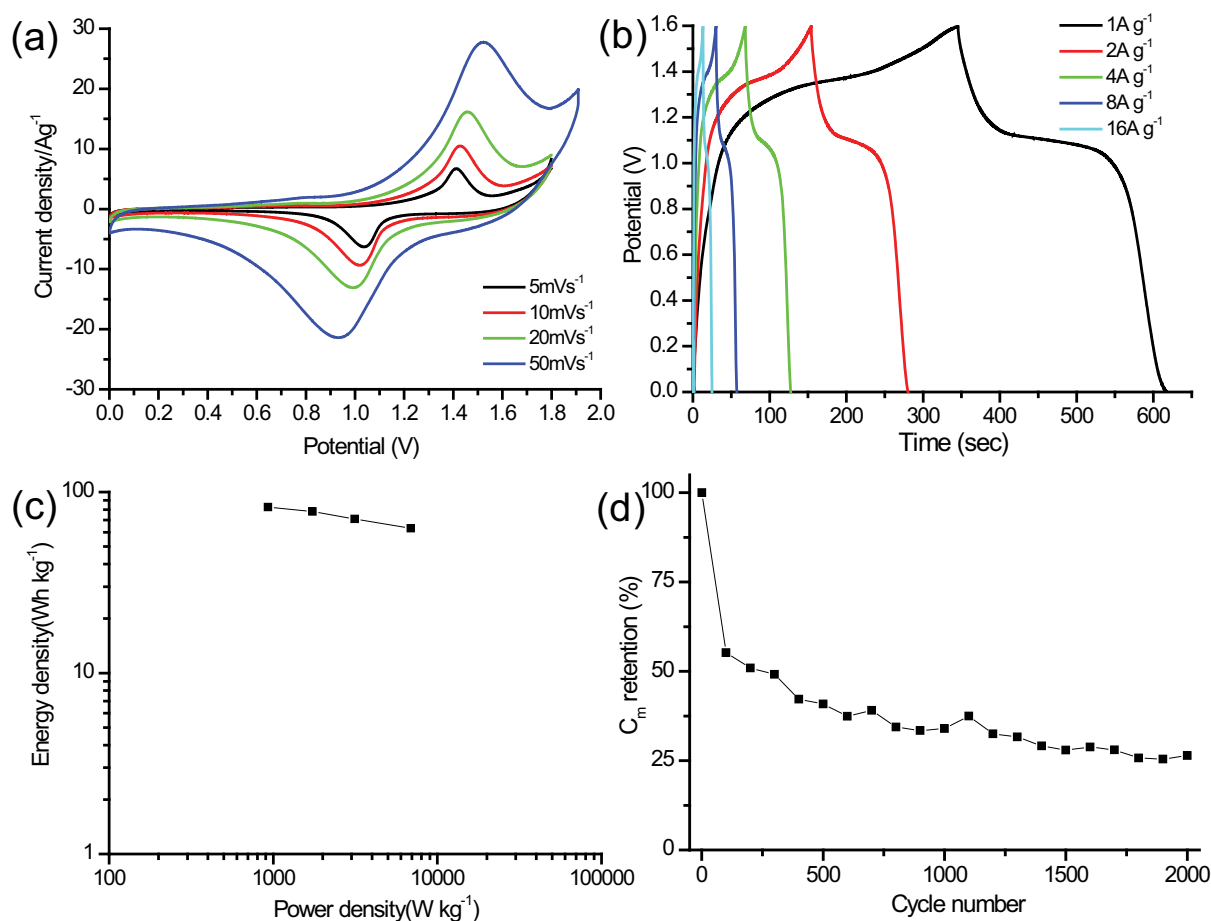**Figure 7 | Electrochemical performances of an ASC.** (a) CV curves of the NiOOH/Ni$_3$S$_2$/3D-G//Fe$_3$O$_4$/rGO device collected at the different scan rates (5, 10, 20 and 50 mV/s). (b) Galvanostatic charge/discharge curves of the NiOOH/Ni$_3$S$_2$/3D-G//Fe$_3$O$_4$/rGO device recorded at different current densities (1, 2, 4, 8 and 16 A/g). (c) Ragone plot of the NiOOH/Ni$_3$S$_2$/3D-G//Fe$_3$O$_4$/rGO device. (d) The capacitance retention of the NiOOH/Ni$_3$S$_2$/3D-G//Fe$_3$O$_4$/rGO device as a function of cycle number at a current density of 1 A/g.

anode is not maintained, which further impairs the capacitive performance of NiOOH/Ni$_3$S$_2$/3D-G//Fe$_3$O$_4$/rGO device. Very recently, Long et al. have reported that the high capacitance of graphene supported iron nanosheets is mainly attributed to electrochemical transformation from Fe to Fe$_3$O$_4$ under alkaline condition[48]. In their cycling test, the composite anode shows a significant decrease in capacitance. This instability could be mainly associated with the aggregation of Fe$_3$O$_4$ particles during electrochemical cycles, resulting in the loss of bonding between Fe$_3$O$_4$ and the graphene sheets, and the subsequent loss of the electrochemical activity. Because our TEM observation on Fe$_3$O$_4$/rGO electrode after 2000 charge/discharge cycles is consistent with the scenario reported by Long et al. (Figure S7c), we use gel electrolyte to improve the electrochemical stability of Fe$_3$O$_4$/rGO electrode[59]. The encapsulation of Fe$_3$O$_4$/rGO electrode within gel electrolyte should be able to prevent the separation of Fe$_3$O$_4$ nanoparticles from rGO substrate. We thus examine the cycling performance of Fe$_3$O$_4$/rGO electrode in a gel electrolyte and compare it to the values obtained in an aqueous electrolyte. As shown in Figure S8c, the capacitance of Fe$_3$O$_4$/rGO electrode decreases continuously in a 1 M KOH solution and only 38% of the initial capacitance is retained after 1000 cycles. In contrast, the capacitance of Fe$_3$O$_4$/rGO electrode decreases slowly in the gel electrolyte and more than 70% of the initial capacitance is retained after 1000 cycles. Although Fe$_3$O$_4$/rGO electrode in a gel electrolyte shows a lower C$_m$ value (287.4 F/g at 1 A/g, Figure S8b), its cycling stability is significantly improved. Searching the ideal composition of gel electrolyte where electrodes without sacrificing their electro-

chemical performances and the assembly of ASC device with gel electrolyte, requiring intense research efforts, are currently under investigation in our group.

Discussion

We have successfully synthesized hierarchically structured Ni$_3$S$_2$/3D-G composites using glucose-assisted hydrothermal method. The Ni$_3$S$_2$ nanoparticles are densely and uniformly grown on the surface of 3D-G serving as the porous and conductive substrate. It is found that the use of glucose in hydrothermal reaction is essential to the formation of this hybrid structure. As evidenced by SEM observations, the morphology of Ni$_3$S$_2$/3D-G becomes very rough after the composite electrode is activated by the consecutive CV scanning in a 1 M KOH solution. On the basis of XPS data, we have confirmed that the change in electrode morphology and the capacitance enhancement after the activation process can be attributed to the combined effect of the partial removal of amorphous carbon and the formation of NiOOH. Therefore, the partial removal of amorphous carbon from the electrode surface leads to the increase in the exposure of the active sites in the composite electrode, which further enhances the capacitive performance of composite electrode. Furthermore, the systematic CV measurements have verified that the NiOOH/Ni$_3$S$_2$/3D-G electrode shows the higher capacitive performance and better ion diffusion compared with the pure Ni$_3$S$_2$ electrode. The enhancement of capacitive performance of NiOOH/Ni$_3$S$_2$/3D-G can be attributed to the facts that the highly conductive graphene ensures rapid charge transfer and the small sizes of Ni$_3$S$_2$ nanoparticles on 3D-G allow nearly full utilization of the electrode

materials. On the other hand, the improved ion diffusion can be ascribed to that the open pore system of the composite electrode makes electrolyte fully access to Ni_3S_2. Furthermore, EIS measurements reveal that the $NiOOH/Ni_3S_2/3D$-G has the lower R_s and R_{ct} values than the pure Ni_3S_2 electrode, which further suggests that 3D porous and conductive graphene network is beneficial to electrochemical performance of supercapacitor electrode. Due to the synergistic effects of the electrochemically active nanoparticles and conductive 3D-G, the $NiOOH/Ni_3S_2/3D$-G electrode exhibits the high capacitance of 3296 F/g and great cycling stability at a current density of 16 A/g.

To obtain the reasonable matching of cathode/anode in an ASC device, we have synthesized highly capacitive Fe_3O_4/rGO composite using a hydrothermal method. Fe_3O_4 nanoparticles with the averaged diameter of 5 nm are densely and homogeneously dispersed onto the rGO surface. The Fe_3O_4/rGO electrode exhibits the high capacitance of 661 F/g at 1 A/g and great rate capability. More importantly, an ASC fabricated by using the $NiOOH/Ni_3S_2/3D$-G as the cathode and Fe_3O_4/rGO as the anode exhibits an ultrahigh energy density. The $NiOOH/Ni_3S_2/3D$-G//Fe_3O_4/rGO device can be reversibly charged/discharged at a maximum cell voltage of 1.6 V and a maximum capacitance of 233 F/g can be achieved at a scan rate of 5 mV/s, which delivers a maximum energy density of 82.5 Wh/kg at a power density of 930 W/kg. Such excellent capacitive performance suggests that $NiOOH/Ni_3S_2/3D$-G//Fe_3O_4/rGO device shows a great potential application as an inexpensive energy storage system.

Methods

Synthesis of 3D-G. The 3D-G was synthesized by CVD using nickel foam (1 cm²) as an interconnected 3D scaffold. The nickel foams were heated to 1000°C in a horizontal tube furnace under 10% H_2 (400 s.c.c.m.) and annealed for 30 min to remove a thin surface oxide layer. Then, 10% H_2 (100 s.c.c.m.) and the mixed gases (100 s.c.c.m.) were introduced into the reaction tube. The growth of 3D-G was performed for 30 min under the pressure of 10 torr. Finally, the sample was cooled to room temperature under 10% H_2 (100 s.c.c.m.). Typically, the weight of 3D-G on Ni foam ranged from 0.6 to 0.8 mg.

Synthesis of $Ni_3S_2/3D$-G and Fe_3O_4/rGO. For the synthesis of $Ni_3S_2/3D$-G, glucose (90 mg) was added to the mixture solution of ethanol (9 ml) and distilled water (1 ml). The mixed solution was sonciated for 20 min to make a homogeneous solution and then nickel chloride (48.6 mg), thiourea (19 mg) and 1 ml of ammonia were added to the solution. The solution was transferred to a Teflon-lined stainless steel autoclave (20 ml capacity) and then a piece of 3D-G on nickel foam (1 cm²) was immersed into the autoclave. After sealing, the autoclave was heated to 180°C for 12 h and then cooled to room temperature. Finally, the resulting $Ni_3S_2/3D$-G was washed with distilled water and dried in air. In a separate experiment, the Ni_3S_2 powder was synthesized also using glucose-assisted hydrothermal method. Except the addition of 3D-G, the synthetic procedures for Ni_3S_2 powder were the same as those for $Ni_3S_2/3D$-G.

For the preparation of the material for anode, Fe_3O_4/rGO composite was synthesized based on the previous literature[60]. In brief, $FeCl_3.6H_2O$ (5 mg) and $FeCl_2.4H_2O$ (2 mg) was added to the GO dispersion of 10 mL (a concentration of 0.25 mg/mL) and the mixed solution was stirred overnight at 70°C to make a homogeneous solution. Then 1.5 mL NH_3 solution was added into the solution and the mixed solution was transferred to a Teflon-lined stainless steel autoclave (20 ml capacity). After sealing, the autoclave was heated to 150°C for 2 h and then cooled to room temperature. Finally, the resulting product was washed with distilled water and dried in air. In the separate experiment, the Fe_3O_4 powder was synthesized by following the synthetic procedures of Fe_3O_4/rGO except the addition of graphene oxide. Furthermore, rGO powder is synthesized by a simple hydrothermal method. In brief, graphene oxide (20 mg) synthesized by a modified Hummer's method was added to the mixture solution of ammonia (1.5 ml) and distilled water (10 ml)[8]. The mixed solution was transferred to a Teflon-lined stainless steel autoclave (20 ml capacity) and then the autoclave was heated to 150°C for 2 h. Finally, the resulting product was washed with distilled water and dried in air.

Material characterizations. The surface morphology of $Ni_3S_2/3D$-G was characterized using a field emission scanning electron microscope (JSM-7000F). Field-emission transmission electron microscope (JEOL JEM-2100F, operated at 200 kV with a point-to-point resolution of 0.19 nm) equipped with an energy dispersive spectrometer was used to obtain the information on the microstructures and the chemical compositions. XRD patterns of the composites were obtained from Philips X'Pert Pro MPD. The Raman measurements were performed using a confocal Raman spectroscopic system (Horiba Jobin Yvon) with 532 nm excitation laser and a

50× objective. XPS measurements were carried out with a PHI VersaProbe XPS Microprobe with monochromatic Al K_α X-ray radiation.

Electrochemical measurements. All electrochemical measurements were performed in a standard three-electrode cell. The composite electrode served as the working electrode, while a Pt wire and an Ag/AgCl (sat.KCl) electrode were used as the counter and a reference electrode, respectively. CV and galvanostatic charge–discharge curves were measured in a 1 M KOH solution using a CHI 635A electrochemical workstation. EIS measurements were conducted with an Eco Chemie Autolab PGSTAT-128N potentiostat equipped with the FRA2 frequency response analyzer module and GPES/FRA software. An AC voltage with 5 mV amplitude in a frequency range of 0.01 Hz–10 kHz was applied. For the electrode preparations of Ni_3S_2, rGO, Fe_3O_4 or Fe_3O_4/rGO, the individual powder was mixed with carbon black and polyvinylidene difluoride at a weight ratio of 8 : 1 : 1. After thorough mixing, the slurry was pressed onto Ni foam (1 cm²) and then dried at 60°C in vacuum for 1 day. The as-fabricated electrode was characterized in a 1 M KOH solution using CV and EIS.

Preparation of KOH/PVA gel electrolyte. The powder of polyvinyl alcohol (PVA, 1 g) was dissolved in 10 mL of 1 M KOH solution at 80°C with stirring. After the solution was cooled to room temperature, Fe_3O_4/rGO electrode, a Pt wire and an Ag/AgCl (sat.KCl) electrode were immersed in the solution. Finally, the solution became a clear and transparent gel after it was dried at 40°C in air.

Fabrication of ASC devices. To fabricate the ASCs, Fe_3O_4/rGO and $Ni_3S_2/3D$-G were used as the anode and the cathode, respectively. Two electrodes where the total mass loading of active materials 1.3 mg were separated by a filter paper. The cell was encapsulated by flexible plastic film with two pieces of platinum wires connected to the edges of the two electrodes. Finally, a 1 M KOH solution was injected into the cell to rinse the filter paper. The electrochemical properties of the ASC devices were measured using a CHI 635A electrochemical workstation.

1. Dai, L. Functionalization of graphene for efficient energy conversion and storage. *Acc. Chem. Res.* **46**, 31–42 (2013).
2. Wang, D. W., Li, F., Liu, M., Lu, G. Q. & Cheng, H. M. 3D aperiodic hierarchical porous graphitic carbon material for high-rate electrochemical capacitive energy storage. *Angew. Chem. Int. Ed.* **47**, 373–376 (2008).
3. Liang, Y. *et al.* An advanced carbonaceous porous network for high-performance organic electrolyte supercapacitors. *J. Mater. Chem. A* **1**, 7000–7005 (2013).
4. Liang, Y. *et al.* Construction of a hierarchical architecture in a wormhole-like mesostructure for enhanced mass transport. *Phys. Chem. Chem. Phys.* **13**, 8852–8856 (2011).
5. Xu, F. *et al.* Fast ion transport and high capacitance of polystyrene-based hierarchical porous carbon electrode material for supercapacitors. *J. Mater. Chem.* **21**, 1970–1976 (2011).
6. Zhong, H., Xu, F., Li, Z., Fu, R. & Wu, D. High-energy supercapacitors based on hierarchical porous carbon with an ultrahigh ion-accessible surface area in ionic liquid electrolytes. *Nanoscale* **5**, 4678–4682 (2013).
7. Liang, Y., Wu, D. & Fu, R. Carbon microfibers with hierarchical porous structure from electrospun fiber-like natural biopolymer. *Sci. Rep.* **3**, 1119 (2013).
8. Su, C. Y. *et al.* Electrical and spectroscopic characterizations of ultra-large reduced graphene oxide monolayers. *Chem. Mater.* **21**, 5674–5680 (2009).
9. Stoller, M. D., Park, S. J., Zhu, Y. W., An, J. H. & Ruoff, R. S. Graphene-based ultracapacitors. *Nano Lett.* **8**, 3498–3502 (2008).
10. Zhu, Y. W. *et al.* Exfoliation of graphite oxide in propylene carbonate and thermal reduction of the resulting graphene oxide platelets. *ACS Nano* **4**, 1227–1233 (2010).
11. Liu, C. G., Yu, Z. N., Neff, D., Zhamu, A. & Jang, B. Z. Graphene-based supercapacitor with an ultrahigh energy density. *Nano Lett.* **10**, 4863–4868 (2010).
12. Hu, C. C., Chang, K. H., Lin, M. C. & Wu, Y. T. Design and tailoring of the nanotubular arrayed architecture of hydrous RuO_2 for next generation supercapacitors. *Nano Lett.* **6**, 2690–2695 (2006).
13. Zhang, H. *et al.* Growth of manganese oxide nanoflowers on vertically-aligned carbon nanotube arrays for high-rate electrochemical capacitive energy storage. *Nano Lett.* **8**, 2664–2668 (2008).
14. Dong, X. C. *et al.* 3D graphene–cobalt oxide electrode for high-performance supercapacitor and enzymeless glucose detection. *ACS Nano* **6**, 3206–3213 (2012).
15. Saravanakumar, B., Purushothaman, K. K. & Muralidharan, G. Interconnected V_2O_5 nanoporous network for high-performance supercapacitors. *ACS Appl. Mater. Interfaces* **4**, 4484–4490 (2012).
16. Liang, L., Liu, J., Windisch Jr, C. F., Exarhos, G. J. & Lin, Y. Direct assembly of large arrays of oriented conducting polymer nanowires. *Angew. Chem. Int. Ed.* **114**, 3817–3820 (2002).
17. Parthasarathy, R. V. & Martin, C. R. Template-synthesized polyaniline microtubules. *Chem. Mater.* **6**, 1627–1632 (1994).
18. Cao, Y. & Mallouk, T. E. Morphology of template-grown polyaniline nanowires and its effect on the electrochemical capacitance of nanowire arrays. *Chem. Mater.* **20**, 5260–5265 (2008).

19. Chang, H. H., Chang, C. K., Tsai, Y. C. & Liao, C. S. Electrochemically synthesized graphene/polypyrrole composites and their use in supercapacitor. *Carbon* **50**, 2331–2336 (2012).

20. Chou, S. W. & Lin, J. Y. Cathodic deposition of flaky nickel sulfide nanostructure as an electroactive material for high-performance supercapacitors. *J. Electrochem. Soc.* **160**, D178–D182 (2013).

21. Zhu, T., Wang, Z. Y., Ding, S. J., Chen, J. S. & Lou, X. W. Hierarchical nickel sulfide hollow spheres for high performance supercapacitors. *RSC Adv.* **1**, 397–400 (2011).

22. Hou, L. R. *et al.* Electrochemically induced transformation of NiS nanoparticles into Ni(OH)$_2$ in KOH aqueous solution toward electrochemical capacitors. *Electrochim. Acta* **56**, 7454–7459 (2011).

23. Wu, Z. S. *et al.* Graphene/metal oxide composite electrode materials for energy storage. *Nano Energy* **1**, 107–131 (2012).

24. Wu, Z. S. *et al.* Anchoring hydrous RuO$_2$ on graphene sheets for high-performance electrochemical capacitors. *Adv. Funct. Mater.* **20**, 3595–3602 (2010).

25. Gao, H. C., Xiao, F., Ching, C. B. & Duan, H. W. High-performance asymmetric supercapacitor based on graphene hydrogel and nanostructured MnO$_2$. *ACS Appl. Mater. Interfaces* **4**, 2801–2810 (2012).

26. Chen, Z. P. *et al.* Three-dimensional flexible and conductive interconnected graphene networks grown by chemical vapour deposition. *Nat. Mater.* **10**, 424–428 (2011).

27. Yoon, J. C., Lee, J. S., Kim, S. I., Kim, K. H. & Jang, J. H. Three-dimensional graphene nano-networks with high quality and mass production capability via precursor-assisted chemical vapor deposition. *Sci. Rep.* **3**, 1788 (2013).

28. Dai, C. S. *et al.* Hierarchically structured Ni$_3$S$_2$/carbon nanotube composites as high performance cathode materials for asymmetric supercapacitors. *ACS Appl. Mater. Interfaces* **5**, 12168–12174 (2013).

29. Ding, S. J., Chen, J. S. & Lou, X. W. Glucose-assisted growth of MoS$_2$ nanosheets on CNT backbone for improved lithium storage properties. *Chem. Eur. J.* **17**, 13142–13145 (2011).

30. Yan, Y. *et al.* Facile synthesis of low crystalline MoS$_2$ nanosheet-coated CNTs for enhanced hydrogen evolution reaction. *Nanoscale* **5**, 7768–7771 (2013).

31. Wang, H. L. *et al.* Mn$_3$O$_4$-graphene hybrid as a high-capacity anode material for lithium ion batteries. *J. Am. Chem. Soc.* **132**, 13978–13980 (2010).

32. Wu, Y. P. *et al.* Efficient and large-scale synthesis of few-layered graphene using an arc-discharge method and conductivity studies of the resulting films. *Nano. Res.* **3**, 661–669 (2010).

33. Cheng, Z., Abernathy, H. & Liu, M. L. Raman spectroscopy of nickel sulfide Ni$_3$S$_2$. *J. Phys. Chem. C* **111**, 17997–18000 (2007).

34. Wei, X. W., Zhu, G. X., Xia, C. J. & Ye, Y. A solution phase fabrication of magnetic nanoparticles encapsulated in carbon. *Nanotechnology* **17**, 4307–4311 (2006).

35. Qiu, W. D. *et al.* Facile Synthesis of Hollow MoS$_2$ microspheres/amorphous carbon composites and their lithium storage properties. *Electrochim. Acta* **117**, 145–152 (2014).

36. Zhou, W. J. *et al.* Ni$_3$S$_2$ nanorods/Ni foam composite electrode with low overpotential for electrocatalytic oxygen evolution. *Energy Environ. Sci.* **6**, 2921–2924 (2013).

37. Biesinger, M. C., Payne, B. P., Lau, L. W. M., Gerson, A. & Smart, R. S. C. X-ray photoelectron spectroscopic chemical state quantification of mixed nickel metal, oxide and hydroxide systems. *Surf. Interface Anal.* **41**, 324–332 (2009).

38. Buckley, A. N. & Woods, R. Electrochemical and XPS studies of the surface oxidation of synthetic heazlewoodite (Ni$_3$S$_2$). *J. Appl. Electrochem.* **21**, 575–582 (1991).

39. Okpalugo, T. I. T., Papakonstantinou, P., Murphy, H., McLaughlin, J. & Brown, N. M. D. High resolution XPS characterization of chemical functionalised MWCNTs and SWCNTs. *Carbon* **43**, 153–161 (2005).

40. Xuan, S. H. *et al.* A facile method to fabricate carbon-encapsulated Fe$_3$O$_4$ core/shell composites. *Nanotechnology* **18**, 035602 (2007).

41. Yan, J. *et al.* Fabrication and electrochemical performances of hierarchical porous Ni(OH)$_2$ nanoflakes anchored on graphene sheets. *J. Mater. Chem.* **22**, 11494–11502 (2012).

42. Wang, D. W., Li, F., Liu, M., Lu, G. Q. & Cheng, H. M. 3D aperiodic hierarchical porous graphitic carbon material for high-rate electrochemical capacitive energy storage. *Angew. Chem. Int. Ed.* **47**, 373–376 (2008).

43. Shi, S. *et al.* Flexible asymmetric supercapacitors based on ultrathin two-dimensional nanosheets with outstanding electrochemical performance and aesthetic property. *Sci. Rep.* **3**, 2598 (2013).

44. Zhu, T., Wu, H. B., Wang, Y. B., Xu, R. & Lou, X. W. Formation of 1D hierarchical structures composed of Ni$_3$S$_2$ nanosheets on CNTs backbone for supercapacitors and photocatalytic H$_2$ production. *Adv. Energy Mater.* **2**, 1497–1502 (2012).

45. Wang, A. M. *et al.* Controlled synthesis of nickel sulfide/graphene oxide nanocomposite for high-performance supercapacitor. *Appl. Surf. Sci.* **282**, 704–708 (2013).

46. Zhang, H. M. *et al.* Synthesis of bacteria promoted reduced graphene oxide-nickel sulfide networks for advanced supercapacitors. *ACS Appl. Mater. Interfaces* **5**, 7335–7340 (2013).

47. Li, H. B. *et al.* Amorphous nickel hydroxide nanospheres with ultrahigh capacitance and energy density as electrochemical pseudocapacitor materials. *Nat. Commun.* **4**, 1894 (2013).

48. Long, C. L., Wei, T., Yan, J., Jiang, L. L. & Fan, Z. J. Supercapacitors based on graphene-supported iron nanosheets as negative electrode materials. *ACS Nano* **7**, 11325–11332 (2013).

49. Li, B., Cao, H., Shao, J., Qu, M. & Warner, J. H. Superparamagnetic Fe$_3$O$_4$ nanocrystals@graphene composites for energy storage devices. *J. Mater. Chem.* **21**, 5069–5075 (2011).

50. Wang, Q. H., Jiao, L. F., Du, H. M., Wang, Y. J. & Yuan, H. T. Fe$_3$O$_4$ nanoparticles grown on graphene as advanced electrode materials for supercapacitors. *J. Power Sources* **245**, 101–106 (2014).

51. Qi, T. *et al.* Synergistic effect of Fe$_3$O$_4$/reduced graphene oxide nanocomposites for supercapacitors with good cycling life. *Electrochim. Acta* **114**, 674–680 (2013).

52. Cheng, J. P. *et al.* Influence of component content on the capacitance of magnetite/reduced graphene oxide composite. *J. Electroanal. Chem.* **698**, 1–8 (2013).

53. Zhu, J. X. *et al.* Hydrogenated CoO$_x$ nanowire@Ni(OH)$_2$ nanosheet core-shell nanostructures for high-performance asymmetric supercapacitors. *Nanoscale* **6**, 6772–6781 (2014).

54. Jin, W. H., Cao, G. T. & Sun, J. Y. Hybrid supercapacitor based on MnO$_2$ and columned FeOOH using Li$_2$SO$_4$ electrolyte solution. *J. Power Sources* **175**, 686–691 (2008).

55. Cottineau, T., Toupin, M., Delahaye, T., Brousse, T. & Belanger, D. Nanostructured transition metal oxides for aqueous hybrid electrochemical supercapacitors. *Appl. Phys. A* **82**, 599–606 (2006).

56. Shanmugavani, A. & Kalai Selvan, R. Synthesis of ZnFe$_2$O$_4$ nanoparticles and their asymmetric configuration with Ni(OH)$_2$ for a pseudocapacitor. *RSC Adv.* **4**, 27022–27029 (2014).

57. Lin, Y. P. & Wu, N. L. Characterization of MnFe$_2$O$_4$/LiMn$_2$O$_4$ aqueous asymmetric supercapacitor. *J. Power Sources* **196**, 851–854 (2011).

58. Ma, S. B. *et al.* A novel concept of hybrid capacitor based on manganese oxide materials. *Electrochem. Commun.* **9**, 2807–2811 (2007).

59. Wang, G. M. *et al.* LiCl/PVA gel electrolyte stabilizes vanadium oxide nanowire electrodes for pseudocapacitors. *ACS Nano* **6**, 10296–10302 (2012).

60. Shi, W. H. *et al.* Achieving high specific charge capacitances in Fe$_3$O$_4$/reduced graphene oxide nanocomposites. *J. Mater. Chem.* **21**, 3422–3427 (2011).

Acknowledgments

Author contributions

T.L. designed and supervised the experiments, analyzed the data and wrote the paper. C.D. performed synthesis experiments, material characterizations, and electrochemical measurements. K.H. conducted the XPS measurements for electrode materials.

Additional information

Supplementary information accompanies this paper at http://www.nature.com/scientificreports

Competing financial interests: The authors declare no competing financial interests.

How to cite this article: Lin, T.-W., Dai, C.-S. & Hung, K.-C. High Energy Density Asymmetric Supercapacitor Based on NiOOH/Ni$_3$S$_2$/3D Graphene and Fe$_3$O$_4$/Graphene Composite Electrodes. *Sci. Rep.* **4**, 7274; DOI:10.1038/srep07274 (2014).